Carbohydrate Polymers 115 (2015) 285–293

Contents lists available at ScienceDirect

Carbohydrate Polymers

journal homepage: www.elsevier.com/locate/carbpol

Biopolymer starch mediated synthetic route of multi-spheres and donut ZnO structures

Oana Carp[a,*], AlinaTirsoaga[b], Bogdan Jurca[b], Ramona Ene[a], Simona Somacescu[a], Adelina Ianculescu[c]

[a] Ilie Murgulescu" Institute of Physical Chemistry, Romanian Academy, Splaiul Independentei 202, 060021 Bucharest, Romania
[b] University of Bucharest, Physical Chemistry Department, Bd. Elisabeta 4-12, 030018, Romania
[c] Politechnica" University of Bucharest, Gh. Polizu Street no.1-7, 011061 Bucharest, Romania

ARTICLE INFO

Article history:
Received 4 November 2013
Received in revised form 22 April 2014
Accepted 10 August 2014
Available online 3 September 2014

Keywords:
Starch
ZnO
Multi-spheres and donut structure
Optical properties, Visible-photocatalyst

ABSTRACT

A starch-assisted synthetic methodology of multispheres ZnO–starch biocomposites was developed. An additional thermal processing of the ZnO–starch composites induces the formation of ZnO with donut-like morphology. The synthesis of single-phase zinc oxide with a spherical morphology is conditioned by the presence of starch, which acts as template, stabilizing/capping agent. The synthesized structures present significant photocatalytic activities; a total phenol mineralization is attained with the donut-like ZnO photocatalyst under visible light irradiation, due to a cumulative effect of the its relatively large specific surface area, high crystallinity and favorable combination of defects for band narrowing, which together permit an enhanced utilization rate of the light.

1. Introduction

In the last decade, the increase receptiveness towards the environment, forced a reinventing of the nanotechnology in a green context (McKenzie & Hutchison, 2004). One of the Green Chemistry principles is the use of renewable raw materials and feedstocks whenever technically and economically practical, rather than depleting non-renewable materials (Anastas & Warner, 1998). Certainly, the biomass is the most renewable feedstock in terms of volume produced (175 billion tons of biomass materials per year), polysaccharides being ~70% of it. Unfortunately, far too little of the produced amounts of polysaccharides are currently used (~4% mainly in food industry), the most decays and recycles along natural pathways (Thoen & Busch, 2006). In these circumstances, finding efficient applications that add supplementary value should represent one of the multidisciplinary research topics of this beginning of the millennium.

Despite their indisputable green attributes (renewability, highly availability, and nontoxic nature) associated with outstanding versatile functionalities, the implication of polysaccharides in the synthesis of different materials (metals, metal oxides, and composites) is an insufficiently explored research issue of materials science (Visinescu, Patrinoiu, Tirsoaga, & Carp, 2013). Among polysaccharides, starch has a special place due to its abundance, low-cost and, properties derived from its two constituents, amylose and amylopectine. The linear and helical-shaped amylose affects particles shape and size development during the synthesis stages due to its gelling assets and capacity to form protective functionalized surroundings around the synthesized nanoparticles (Coperland, Blazek, Salam, & Chiming, 2009). The branched amylopectine assures the biopolymer solubility. Starch hydroxyl groups could be involved in dynamic intra- or intermolecular supramolecular associations (Imberty, Chanzy, Perez, Buleon, & Tran, 1988; Raveendran, Fu, & Wallen, 2003), establishing coordinative bonds with various transitional metal ions (Chang, Yu, Ma, & Anderson, 2011; Thirumavalavan, Huang, & Lee, 2013).

On the other hand, the nontoxic and biocompatible ZnO is one of the most fascinating materials, gathering a plethora of structures and an extraordinary combination of properties and applications. Although TiO_2 is by far the most used photocatalyst, ZnO represents an effective alternative because of its similar band gap (3.37/3.23 eV for ZnO/TiO_2), lower cost and, variety of structures (Liao, Badour, & Liao, 2008; Xu et al., 2009).

In general, there are two ways to *design*/synthesize ZnO nanostructures: vapor-phase processes and solution chemical routes. While the first requires complex processes and sophisticated equipments that noticeably increase the synthesis costs, the second alternative has become a promising option for large-scale

* Corresponding author. Tel.: +40 0213121149; fax: +40 0213121149.
E-mail address: ocarp@icf.ro (O. Carp).

http://dx.doi.org/10.1016/j.carbpol.2014.08.061
0144-8617/

production due to its simpler, faster, and less costly merits. Additionally, solution routes have an important benefit permitting the use of organic additives as growth inhibitors and crystal habit modifiers that can tune the size and shape of the final products (Lepot et al., 2007; Sounart et al., 2006; Sun et al., 2008; Zeng & Yang, 2006). In addition, if the additive is a renewable material, the synthesis shifts from a conventional route to a green one. Hitherto, several studies report the synthesis of ZnO in the presence of polysaccharides such as starch (Mumalo-Djokic, Stern, & Taubert, 2008; Vigneshwaran, Kumar, Kathe, Varadarajan, & Prasad, 2006), cellulose derivatives (Bobowska, Wojciechowski, & Halamus, 2008; Kamalasanan & Chandra, 1996; Yin et al., 2010), alginate (Baskoutas, Giabouranis, Yannopoulos, & Dracopoulos, 2007; Gao et al., 2006; Trandafilović, Božanić, Dimitrijević-Branković, Luyt, & Djoković, 2012), and chitosan (Li, Wu, & Zhitomirsky, 2010). The phase purity, shape and size distribution of the obtained ZnO depend strongly on the polysaccharides nature and adopted synthesis parameters.

The objective of the present paper is to demonstrate that starch may be used successfully as green additive in metal oxides synthesis. The biopolymer plays a decisive role in the synthesis of single-phase metal oxide with particular 3-D spherical architectures. Moreover, the synthesis methodology is not sensitive to starch's amylose/amylopectine content and oxidation degree (in the investigated ranges), allowing the use of the biopolymer from different sources and/or batches. Customizing for ZnO the synthetic procedure, a simple starch-assisted synthetic route led to multi-spheres ZnO morphologies, which upon heating are converted to donut-like ZnO structures. The obtained materials are characterized by interesting optical properties and high photocatalytic performances tested for the phenol degradation reaction in an aqueous solution.

2. Experimental

2.1. Materials

All chemicals (analytical grade) were used as received: soluble oxidized corn starch (Carl Roth, Germany), zinc acetate dihydrate [$Zn(CH_3COO)_2{\cdot}2H_2O$, Reactivul, Romania] and ammonia aqueous solution (Chimopar, Romania). The utilized starch presents an amylose/amylopectine ratio equal with 26/74, and a carbonyl and carboxyl content of <0.1% (Kaukpetoom & Wang, 2001) and <0.35% (ISO-11214-1996 method), respectively. Remark: the same results concerning the ZnO–starch composite and its derived oxides were obtained using starch polymers with an amylose content ranging from 20% to 29%.

2.2. Synthesis procedure

A total of 0.324 g starch was dissolved in 110 mL hot water under stirring till a clear solution is formed. In order to obtain an AGU/zinc acetate (AGU = anhydroglucose unit) molar ratio equal with 0.5, the cooled starch solution was mixed with 50 ml of zinc acetate solution (0.878 g). Maintaining the stirring, an aqueous solution of ammonia (2.88 M) was added drop wise till a pH value of 10.35 is attained. The reaction mixture was held under continuous stirring at 80 °C for 150 min. Afterward, the white colloidal solution was centrifuged, the isolated product washed several times with distilled water and dried on P_4O_{10}. The obtained starch–ZnO composite was noted as ZnO_C. To get pure ZnO phase, the composite was calcinated in air with a heating rate of 10 °C/min for 1 h at 500 °C (ZnO_500) and 800 °C (ZnO_800), respectively.

2.3. Characterizations

The crystalline structure of the obtained products was analyzed by *X-ray diffraction* (XRD) carried out at room temperature with a SHIMADZU XRD 6000 diffractometer, using Ni-filtered Cu Kα radiation ($\lambda = 1.5418$ Å) for 2θ ranging between 20° and 80°. The crystallites size was estimated for the three main peaks of ZnO [(1 0 0), (0 0 2), (1 0 1)] using Scherrer equation. The morphology of the as-synthesized samples was investigated by *scanning electron microscopy* (SEM) using a Quanta 3D FEG microscope and by *transmission electron microscopy* (TEM and HRTEM) coupled with SAED (selected area electron diffraction) and EDX (energy dispersive X-ray spectroscopy) using a TECNAI F30 S-Twin microscope. *Thermal measurements* were performed on a Q-1500 Paulik-Paulik-Erdey derivatograph in static air, with a heating rate of 10 °C/min and a sample mass of ~50 mg. *The BET surface area, total pore volume* and *pore size distribution* were obtained with a Micromeritics ASAP 2020 automated gas adsorption system. *Infrared spectra* (FTIR) were recorded from KBr pellets on a FTIR Brucker Tensor V-37 spectrophotometer. *UV–vis spectra* were recorded with a JASCO V-670 spectrophotometer in the range 200–1000 nm. *Photoluminescence measurements* (PL) were performed on a JASCO FP 6500 spectrophotometer, using 350 nm excitation line of xenon light. Room temperature *Raman* spectra were recorded in the range from 70 to 2000 cm^{-1} using a Horiba Jobin-Yvon LabRam HR spectrometer and the green line on an Ar+ laser ($\lambda = 514.5$ nm). *X-ray photoelectron spectroscopy* (XPS) was carried out on a PHI Quantera equipment with a base pressure in the analysis chamber of 10^{-9} Torr. The X-ray source was monochromatized Al Kα radiation (1486.6 eV) and the overall energy resolution is estimated at 0.65 eV by the full width at half-maximum of the Au 4f7/2 photoelectron line (84 eV). Although the charging effect was minimized by using a dual beam (electrons and Ar ions) as neutralizer, the spectra were calibrated using the C1s line (BE = 284.8 eV).

2.4. Photocatalytical activity

The phenol degradation was investigated in stationary quartz reactors with UV (60 W, filter at $\lambda = 365$ nm) and visible (60 W, $\lambda > 380$ nm) lamps and a distance between the light source and reaction tube of 8 cm. The reactions were carried out in the glass mini reactors (5 mL) at 20 °C, using 0.05 g of catalyst and 3 mL of phenol solution 2×10^{-3} M. In order to reach adsorption–desorption equilibrium, prior to irradiations, the aqueous solutions of phenol were 30 min magnetically stirred in dark. In all the experiments the reactors were maintained under continuous magnetic stirring at room temperature for 5 h. The reaction products filtered through Millipore membrane filters were analyzed on a DANI GC 1000 gas chromatograph connected to a FID detector with capillary column OPTIMA-1 (diameter = 0.32 mm, film thickness = 0.5 μm, and length = 30 m). The conversion (c) and mineralization (m) were calculated by using the equations $c = (C_0 - C)/C_0$ and respectively $\min = (C_0 - C_{\min})/C_0$, where C_0, C, and $C_{\min}$ are the toluene concentrations before irradiation, after a certain irradiation time, and the organic compounds concentration after a certain irradiation time.

3. Results and discussions

A simple basic, starch-assisted hydrolysis of zinc acetate was performed at 80 °C as described in the Experimental Section. A white turbidity appear as early as 20 min of heating treatment, but yields higher than 50% are obtained only after 90 min of reaction; at 150 min more than 90% of the zinc acetate is converted into ZnO. It is important to mention that the phase composition and the morphology of the final products are preserved during the progress of the synthesis.

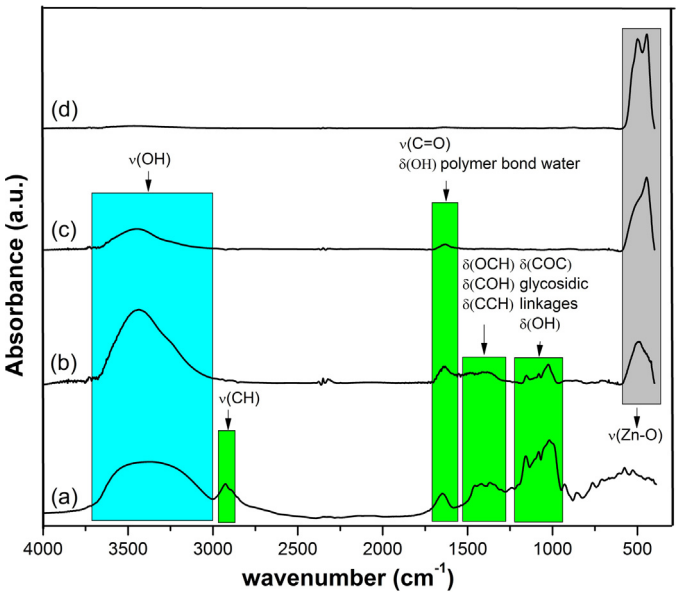

Fig. 1. FTIR spectra of (a) starch; (b) ZnO–starch composite; (c) ZnO_500, and (d) ZnO_800.

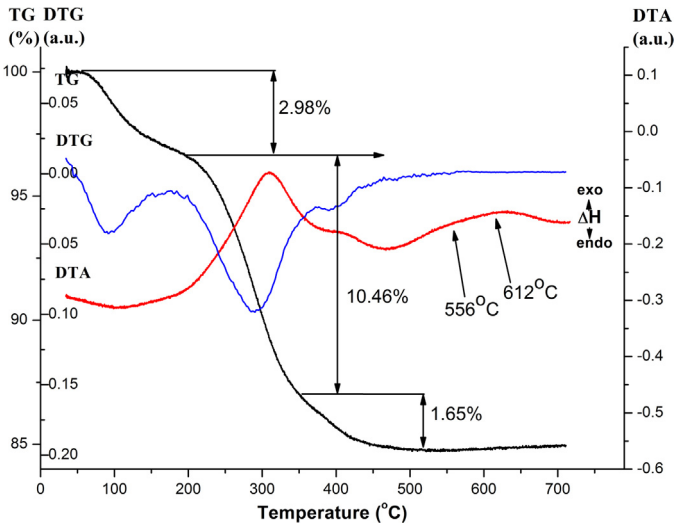

Fig. 2. Thermal curves (TG, DTG, and DTA) of ZnO_C.

3.1. Reaction products characterization

The IR investigations of the ZnO_C composite [Fig. 1(b)] reveal beside the formation of ZnO, the presence of bonded water and starch [almost all starch [Fig. 1(a)] fingerprints are discerned]. An interesting evolution of the $\nu_{(OH)}$ vibration from ~3440 cm^{-1} assigned to chemisorbed and/or physisorbed water molecules and/or hydroxyl groups may be noticed: if in the case of neat starch the band is very broad, for ZnO_C composite it turned narrower due to a certain ceasing of the hydrogen bonds as a result of hydroxyl groups involvement in linkages with zinc ions. ZnO mineralization is sustained by the strong absorption band from 493 cm^{-1} that corresponds to Zn—O stretching vibrations (Nakamoto, 1986). The evolving of starch and water during calcination is supported by the disappearance of their main IR peaks; a very weak band assigned to the $\nu_{(C=O)}$ vibration together with a medium one attributed to $\nu_{(OH)}$ vibration, both derived from a persistent carbonaceous residue are identified only for ZnO_500 [Fig. 1(c)].

The thermal behavior of ZnO_C is presented in Fig. 2. The first decomposition stage (56.4–174.4 °C) corresponds to the evolving of surface bonded water and the following two decompositions (174.4–369.3 °C and 369.3–489.1 °C) to the starch oxidative degradation (Jurca, Tirsoaga, Ianculescu, & Carp, 2014). From the thermogravimetric data, a molar composition equal with 14ZnO–1AGU–2H_2O may be advanced for the composites isolated at different reaction times. Such an assessment may be formulated because the oxidized starch does not retrograde, and therefore no sedimentation of soluble components is expected during the centrifugation step (Belitz, Grosch, & Schieberle, 2009). The starch contained by composite decomposes at considerably lower temperatures (with ~160 °C) comparative with pure starch. Such a substantial variation of the biopolymer thermal stability is caused by a disturbance of the initial intra- and intermolecular associations due to the participation of the hydroxyl groups in linkages with Zn^{2+}, which results in concordance with FTIR data also. Nevertheless, a catalytic effect of ZnO cannot be entirely excluded. The large exothermic effect (476.3–697.5 °C) that follows the mass loss stages is assigned to the nucleation and growth processes of ZnO crystallites (Marinkivic, Mancic, & Milosevic, 2004).

The XRD patterns of the three samples are characteristic for ZnO with a wurtzite structure [Fig. 1(a)–(c) Electronic Supplementary material]. The absence of starch diffraction peaks is an indication that the biopolymer contained by ZnO_C composite is amorphous [Fig. 1(a) Electronic Supplementary Material]. The thermal processing of the ZnO_C composite determines an increase of ZnO crystallites sizes, the augmentation being more pronounced along the *a*-axis (Table 1). Such an unusual large increment of the size with temperature is caused by the disappearance of the steric hindrance imposed by starch and, by the sintering processes that take place at this temperature. It is also worth mentioning, that in absence of starch, the reaction product is mainly $Zn(OH)_2$ with traces of ZnO (Fig. 2 Electronic Supplementary Material), the key role played by starch in the developed synthesis being obvious.

The formed phases were also investigated by Raman spectroscopy (Fig. 3). In ZnO_C spectrum the peaks of starch (Łabanowska, Wesełucha-Birczyńska, Kurdziel, & Puch, 2013) can be found besides ZnO ones. The dominant, strong Raman band obtained at 437 cm^{-1} characteristic for ZnO wurtzite is assigned to the nonpolar optical phonon E_2 modes at high frequency (Cao, Cai, Li, Sun, & Zhang, 2005; Jiang et al., 2007). Its width (<8 cm^{-1}) indicates a good crystal quality for all three ZnO structures (Li, Xiong, & Xie, 2005). The less prominent peaks at 332 and 385 cm^{-1} are attributed to the secondary Raman scattering aroused from zero-boundary phonons 2-E_2 and polar

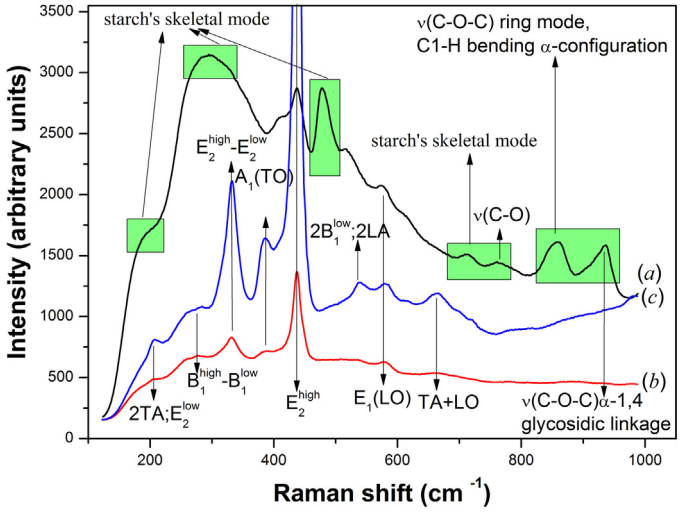

Fig. 3. Raman spectra of (a) ZnO_C composite; (b) ZnO_500, and (c) ZnO_800.

Table 1
Structural, morphological and photocatalytical data of ZnO_C composite, ZnO_500, and ZnO_800.

Sample	$D_{(100)}$ *a*-axis (Å)	$D_{(002)}$ *c*-axis (Å)	$D_{(101)}$ (Å)	$D_{(100)}/D_{(002)}$	S_{BET} ($m^2\ g^{-1}$)	V_{total} ($cm^3\ g^{-1}$)	Pore size (nm)	Phenol photocatalytical conversions			
								UV		Visible	
								Con.[a]	Min.[b]	Con.	Min.
ZnO_C	111	137	111	0.80	7.76	0.0427	25.27	93.5	68.5	73.5	69.5
ZnO_500	237	244	222	0.97	14.55	0.0960	23.79	89.4	89.4	100	100
ZnO_800	362	370	350	0.97	3.63	0.0125	49.95	95.3	72.5	92.1	87.0

[a] Con. = conversion (100%).
[b] Min. = mineralization (100%).

transverse A_1 optical phonon mode, respectively. A low-intensity peak is observed as well at 207 cm^{-1}, being assigned to an associated contribution of 2TA and low-E_2 modes. The three peaks, positioned at 539, 579, and 664 cm^{-1} are attributed to low-$2B_1$ and LA overtone A_1(LO), E_1(LO), and TA + TO combination correspondingly. The E_1(LO) vibration associated with the presence of defects as oxygen vacancies, zinc interstitials and/or their combination (Decremps, Pellicer-Porres, Saitta, Chervin, &

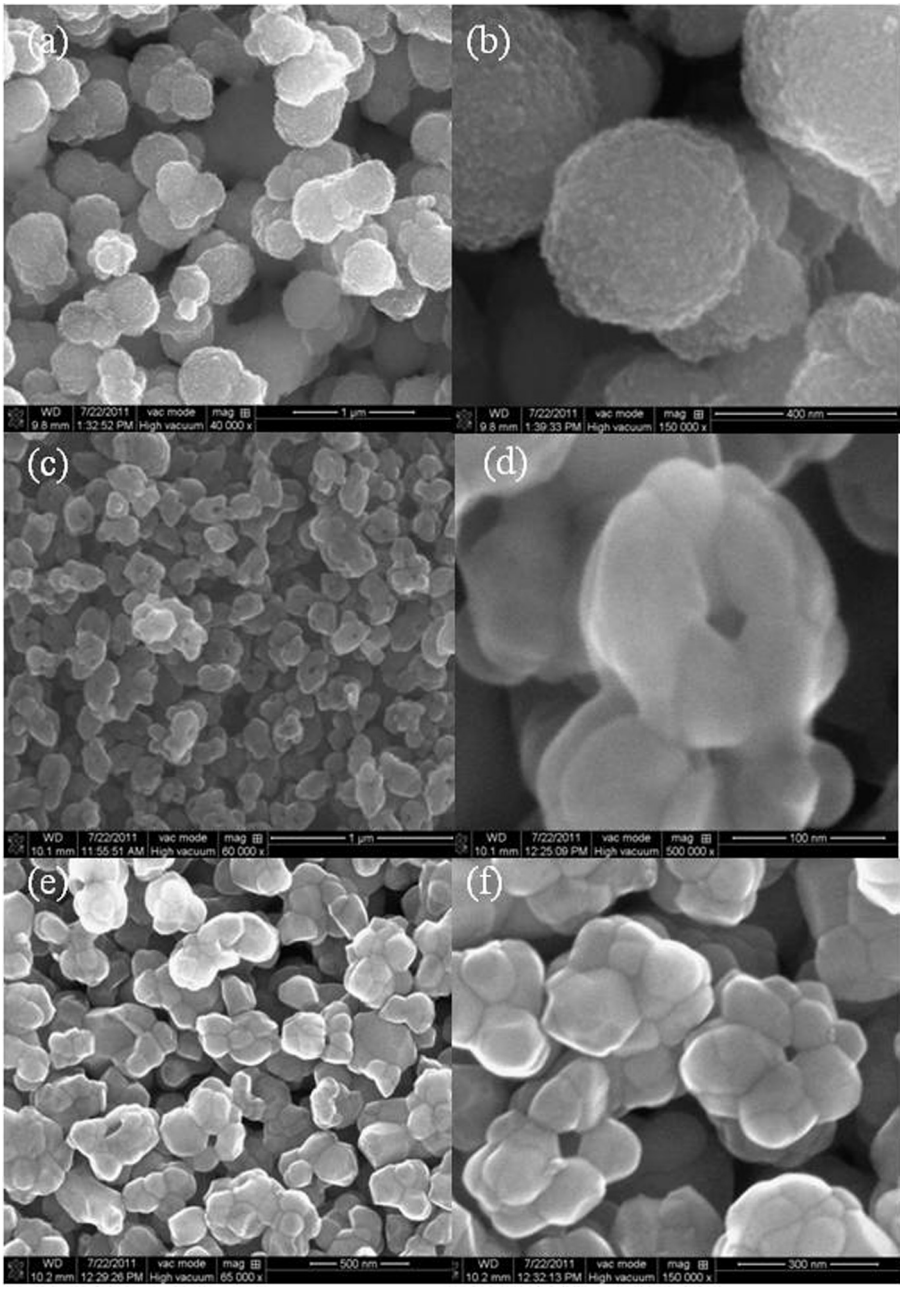

Fig. 4. SEM micrographs of (a, b) ZnO_C composite, (c, d) ZnO_500, and (e, f) ZnO_800.

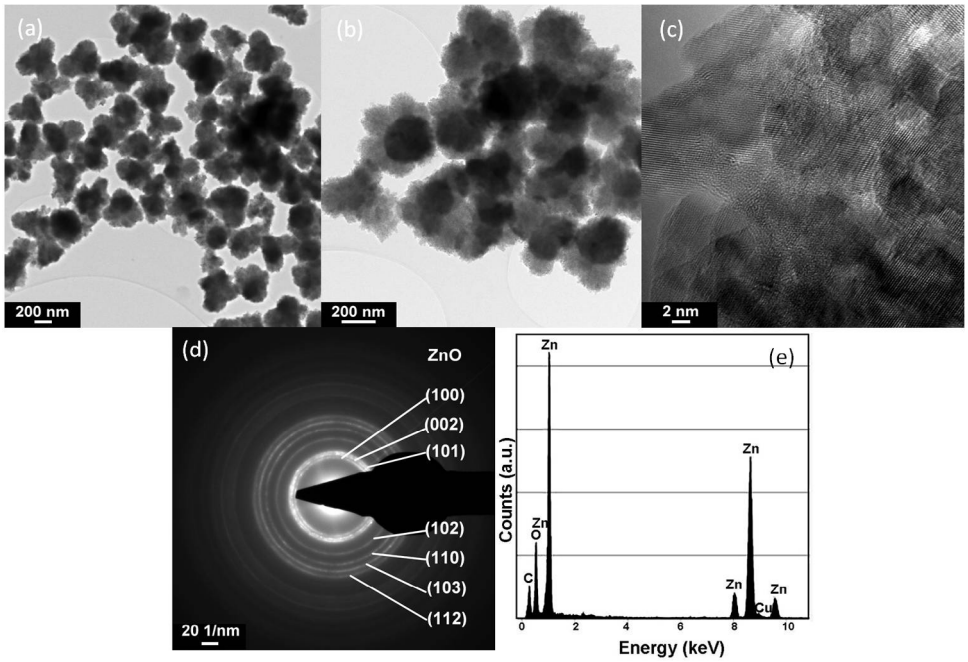

Fig. 5. TEM/HRTEM images of the ZnO_C composite sample: (a) lower magnification TEM image indicating clusters formed as a result of a peculiar self-assembly phenomenon of ZnO spheres; (b) higher magnification TEM image showing the rough surface of ZnO spheres; (c) HRTEM image showing small, polyhedral crystallites of dissimilar orientation inside of a ZnO mesocrystal; (d) SAED pattern corresponding to (a) and (e) EDX spectrum.

Polian, 2002) presents a stronger intensity in ZnO_C and ZnO_800 samples.

The surface characteristics are noticeably influenced by the thermal processing also. The calcination of the composite at 500 °C determines a doubling of the specific surface area due to the evolving of starch and surface bonded water (Table 1). A further increase of the temperature (800 °C) decreases the specific surface area to a value lower even than that of the composite's one, behavior assigned to a partial sintering process. According to the BJH pore size distribution curve calculated from the desorption isotherm (Fig. 4 Electronic Supplementary Material), the composite and ZnO_500 sample present a similar average pore diameter (Table 1), but ZnO_500 has a significant lager total pore volume as a consequence of its cleaner surface. For the sample ZnO_800 the average pore diameter is at the upper limit of the range characteristic for mesoporous materials, the porosity of this sample presumably arise from the interparticles spaces.

From a morphological point of view, the composite obtained even at the beginning of their precipitation consist in clusters of 5–7 spheres characterized by a rough surface and diameters ranging from 100 to 500 nm [Fig. 4(a) and (b)]. A considerably modification of the morphology is attained after calcination: the multi-spheres aggregates flatten and change into donuts-shaped morphologies [Fig. 4(c) and (d)]. The diameters of the entire new formed structure vary between 150 and 550 nm, and a round centered-located hole of 15–35 nm crosses it transversely. With temperature rising, a shrinkage of the hole diameter is noticed [Fig. 4(e) and (f)].

In addition to the SEM investigations, TEM analysis of the ZnO_C composite clearly indicates the same peculiar self-assembly phenomenon of ZnO spheres into clusters [Fig. 5(a) and (b)]. The higher magnification image [Fig. 5(b)] suggests that the rough surfaces of the spheres is most likely due to their polycrystalline nature. Indeed, the HRTEM image inside of a ZnO_C composite sphere [Fig. 5(c)] points out that actually such a sphere is a mesocrystal consisting of small, polyhedral crystallites with dissimilar orientation and high crystallinity degree as proved by the ordered fringes corresponding to the crystalline planes of ZnO. The size of these crystallites estimated from several HRTEM images is ranged between 10 and 15 nm, which is consistent with the average crystallite size calculated from the XRD data (Table 1). Despite the high crystallinity inside the small crystallites, however, their low size seems to affect somewhat the global long-range order in the architectures of spheres, as revealed by the small and less marked spots forming almost continuous, but well-defined, concentric diffraction rings in the SAED pattern corresponding to Fig. 5(d). The qualitative elemental analysis proves the high purity of the ZnO_C composite, so that only the presence of Zn, O, and C species were detected in the EDX spectrum of this sample, as it has been noticed in Fig. 5(e).

The XPS spectra of the calcinated samples [Fig. 4(a) and (b) Electronic Supplementary Material] show the presence of zinc, oxygen and small amounts of adsorbed hydrocarbons (<10%). The two peaks obtained by the deconvolution of O 1s one [Fig. 4(c) and (d) Electronic Supplementary Material], are assigned to O^{2-} ions in wurtzite structure (I, ~530.5 eV) and O_x^- ions (O^- and O_2^-) in the oxygen deficient regions (II, ~532.0 eV) (Chen et al., 2000). The contribution of the OH groups confined on the top of the surface cannot be ruled out, particularly for ZnO_500. The temperature rising from 500 to 800 °C induces an increase of the oxygen vacancies, the quantitative analysis (Table 2) estimates a Zn:O ratio close to 1 and equal with 1.41 for ZnO_500 respective ZnO_800 samples. The Zn2p3/2 peak (1021.7 eV) and the Auger ZnLMM transition (498.2 eV) are attributed to wurtzite Zn^{2+} (Fig. 5 Electronic Supplementary Material).

The room-temperature photoluminescence spectra of the three samples (Fig. 6) present an UV band (near band-edge emission) generated by the free-exciton recombination (Greene et al., 2003) and several visible bands covering the violet-red region (deep level emissions) caused by intrinsic/extrinsic defects (Dijken, Meulenkamp, Vanmaekelbergh, & Meijerink, 2000; Djurišić & Leung, 2006). The position of the UV emissions is dependent on the annealing temperature, lying in the sequence ZnO_C < ZnO_800 < ZnO_500 (374 < 383 < 398 nm). As ZnO crystals are properly large for excluding the quantum confinement effect,

Table 2
Summary of XPS data: binding energy, atomic relative concentration.

Sample	Binding energy (eV)					Atomic relative concentration (%)	
	C1s	Zn2p3/2	ZnLMM	O1s (I)	O1s (II)	Zn	O
ZnO_500	284.8	1021.7	498.2	530.5	532.1	49.9	50.1
ZnO_800	284.8	1021.7	498.2	530.5	532.1	58.6	41.4

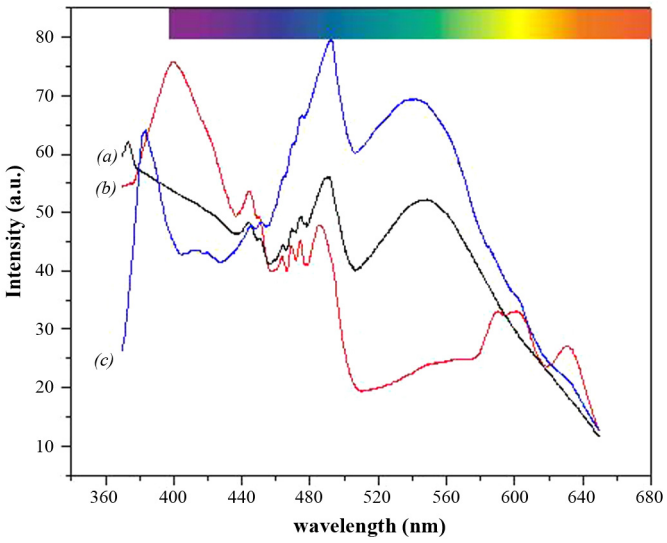

Fig. 6. Room-temperature photoluminescence spectra of (a) ZnO_C composite, (b) ZnO_500, and (c) ZnO_800.

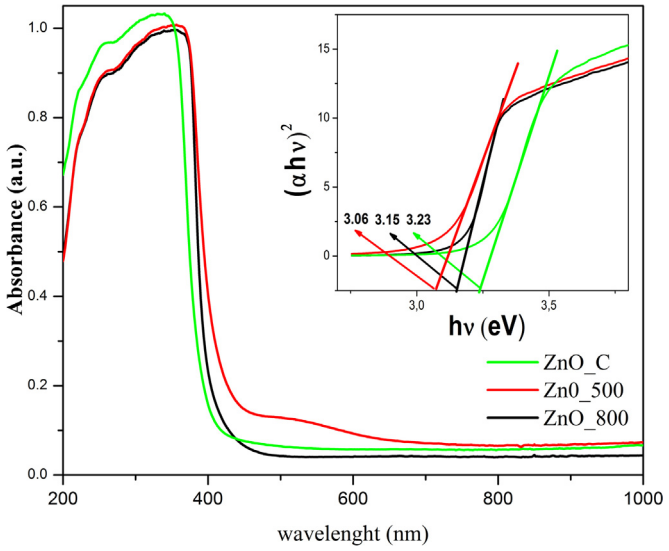

Fig. 7. UV–vis spectra of ZnO_C, ZnO_500, and ZnO_800 and the Tauc plots (inset) where α is the absorption coefficient of ZnO at a certain wavelength, h the Plank's constant and υ the frequency of light.

the variation may be assigned to the difference in morphology and nature and concentration of the native defects that characterized the investigated samples.

The ZnO_C and ZnO_800 spectra show an unexpected resemblance in the visible region, presenting similar blue and green emission peaks, more intense in the case of ZnO_800. In contrast, the ZnO_500 spectrum has a distinct profile, being characterized by weak peaks in the blue range and well-defined bands in the yellow and orange-red ones. The deficiency in oxygen related with blue (Djurišić & Leung, 2006; Zheng et al., 2010) and green emissions (Dijken et al., 2000; Djurišić & Leung, 2006) of the initial composite and ZnO_800 sample has different origins. In the case of ZnO_C composite it is associated with starch presence during the synthesis procedure. Although starch is known as a nonreducing saccharide (Kimball, 1994) this polysaccharide could act as weak reducing agent under specific experimental conditions as proved by its implication as reducing agent in the synthesis of different metals [Te (Lu, Gao, & Komarneni, 2005), Au (Chairam, Poolperm, & Somsook, 2009), and Ag (Vigneshwaran, Nachane, Balasubramanya, & Varadarajan, 2006). Thus, in our case starch induces the formation oxygen vacancies on ZnO surface (a withdrawal of surface oxygen by starch), behavior already identified when other reducing raw materials were used (Liu, Huang, Sulieman, Sun, & He, 2006; Rodriguez-Gattorno et al., 2003; Zheng et al., 2007). During the annealing processes, the formation of oxygen vacancies and oxygen defects are competitive. A thermal treatment performed at 500 °C tend to an adsorption and ionization of the oxygen molecules onto the ZnO surface layers followed by their diffusion toward lattice sites and, as evaluated by XPS investigations a relatively stoichiometric ZnO with interstitial oxygen instead of oxygen vacancy as interface traps is obtained. The presence of the yellow (Greene et al., 2003; Li et al., 2004) and orange-red (Monticone, Tufeu, & Kanaev, 1998; Zheng et al., 2007) emissions supports the affirmation. At higher calcinations temperature (800 °C) it is reasonable to consider two effects: molten zinc redistribution in the solid sample associated with its partial evaporation (zinc melting point = 420 °C) and oxygen adsorption/desorption. The first triggers the formation of zinc vacancies and an increase of interstitial zinc causing the appearance of violet emissions (Djurišić et al., 2006). As concerning the oxygen adsorption/desorption, it seems that for the donut-like particular morphology the oxygen desorption overtakes its adsorption, leading to a deficient zinc oxide (confirmed by XPS data), with a characteristic green emission.

The UV–vis spectra and the Tauc plots of ZnO_C, ZnO_500 and ZnO_800 samples are presented in Fig. 7. Both the absorption edge onset and band gap energy [estimated from $(\alpha h\upsilon)^2$ *vs.* $h\upsilon$ plot according to Tauc relation] are red-shifted comparative with bulk ZnO. While the sequence of the absorption edge onset is ZnO_C < ZnO_800 < ZnO_500 (339 nm < 348 nm < 367 nm), the one obtained for the values of the band gap energy is reverse ZnO_C > ZnO_800 > ZnO_500 (3.23 eV < 3.15 eV < 3.06 eV, Fig. 7 inset). ZnO_500 sample also presents a weak absorption in the visible spectral range (up to ~625 nm), comportment attributed to its morphological peculiarities, although stoichiometry deficiencies and associated defects cannot be completely excluded (Ghoshal, Kar, & Chaudhuri, 2006; Li et al., 2004; Yu, Li, & Liu, 2008).

3.2. Photocatalytic activity

The displayed optical properties (absorption and photoluminescence) of the ZnO architectures indicate their potential toward photocatalytical applications. As test reaction was chosen phenol degradation under UV and visible irradiation. Although so far there are many relative studies reporting phenol photocatalytic degradation under UV light using either TiO_2 or ZnO photocatalyst (Carp, Huismann, & Reller, 2004; Hayat, Gondal, Khaled, Ahmed, & Shemsi,

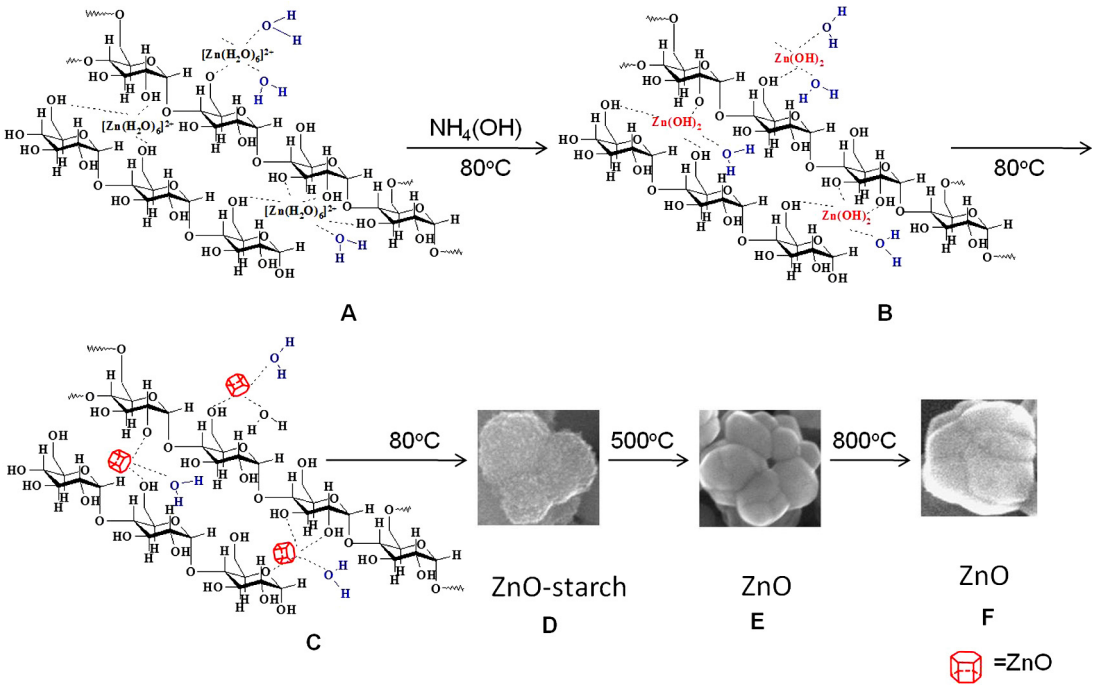

Fig. 8. Schematic illustration on the formation mechanism of multi-spheres and donut-like shaped ZnO.

2011), only few investigations are dedicated to its photocatalytic degradation under visible conditions (Jiang et al., 2011; Wang et al., 2005; Pardeshi & Patil, 2008; Patrinoiu et al., 2012).

The most active photocatalyst is ZnO_500 that shows the best phenol mineralization efficiently (total mineralization under visible irradiation, Table 1). In the case of ZnO_C and ZnO_800 photocatalysts, the main degradation reaction is also the contaminant mineralization, but hydroxylation products (in principal catechol and hydroquinone) that resulted from an incomplete oxidation were identified as well. The recorded phenol conversions for the ZnO_C and ZnO_800 samples are similar in UV conditions, but in visible experiments ZnO_800 has a higher activity.

3.3. *Formation mechanism of ZnO–starch composites and its derived oxides*

The formation of ZnO spherical architectures is rationally proposed to be a starch template mechanism. The nucleation and crystal growth processes of ZnO crystallites are preceded by an induction period during which a Zn^{2+}–starch precursor that directs the space distribution and implicit the dispersion of zinc cations in the system is developed (Fig. 8). The precursor presents catenulate complex structures as a result of coordination, supramolecular, and electrostatic linkages between starch's hydrophilic functional groups and zinc cations (Chang et al., 2011; Somsook et al., 2005),linkages that could include even intermolecular bonds between the individual chains of starch (*i.e.* crosslinking, Fig. 8(a)) (Staroszczyk & Janas, 2010). Subsequently, the addition of the ammonia-water solution converts the initial precursor into a $Zn(OH)_2$–starch one (Wei et al., 2006), that during further heating dehydrates, and ZnO crystals nucleate heterogeneously on the biopolymer surface (Fig. 8(b) and (c)). Starch would not hinder the nucleation of nanocrystals but could restrict the growth rate of the nuclei, thus controlling the size distribution of particles. In order to minimize their surface area (Mo, Yu, & Zhang; Li, 2005), the initial formed ZnO particles attached to the biopolymer, cluster together into colloidal multi-spherical aggregates *via* a self-assembly process. Starch acts probably as a flocculent, driving the aggregation (Zhang & Mu, 2007) (Fig. 8(d)) but also it restrains the further growth of ZnO particles. The dramatic morphology change suffered by the composite during thermal processing is a proof that starch is responsible for the adopted hierarchical structure: its elimination produces the collapse of the multi-sphere aggregates leading to a donut-like structure (Fig. 8(e) and (f)).

4. Conclusions

The starch-assisted developed synthetic procedure represents an example of how a polysaccharide may be transformed into a resourceful additive in oxides synthesis, acting as template and stabilizing/capping agent. The long-chain biopolymer forces the nucleation and growth of ZnO crystallites to occur preferentially on polysaccharides regions of high Zn^{2+} concentrations, controlling also the self-assemblation of ZnO particles into 3-D architectures.

While the initial ZnO–starch composites consist in clusters of 5–7 spheres, a calcination at 500 °C facilitates the change to a donut-like structure whose center-located hole contracts at rising temperatures. The thermal processing leads, at the same time, to a variation of ZnO stoichiometry and implicit associated defects, determining an interesting modulation of the optical properties (absorption edge onset, band gap, and photoluminescence characteristics). Donut-like shaped ZnO exhibits the best photocatalytic performance in phenol degradation; a total mineralization of the contaminant is achieved under visible light irradiation. The behavior may be understood as a result of several simultaneous individualities: a morphology associated with a beneficial combination of defects for band narrowing, a high surface area, and a high total pore volume. This environmentally friendly and facile synthetic route has great potential to extend to other metal oxide synthesis with spherical porous microstructure.

Acknowledgments

This work was supported by a grant of the Romanian National Authority for Scientific Research, CNCS-UEFISCDI, project number

PN-II-ID-PCE-2011-3-0473. The paper was done within the "Green chemistry" research programme of the "Ilie Murgulescu" Institute of Physical Chemistry of the Romanian Academy. Support of the EU (ERDF) and Romanian Government that allowed for acquisition of the research infrastructure under POS-CCE O 2.2.1 project INFRANANOCHEM - Nr. 19/01.03.2009, is gratefully acknowledged.

Appendix A. Supplementary data

Supplementary data associated with this article can be found, in the online version, at http://dx.doi.org/10.1016/j.carbpol.2014.08.061.

References

Anastas, P., & Warner, J. (1998). *Green chemistry: Theory and practice*. Oxford University Press: New York.

Belitz, H. D., Grosch, W., & Schieberle, P. (2009). *Food chemistry* (4th ed., pp. 327). Berlin, Heidelberg: Springer (ISBN 978-3-540-69933-0)

Baskoutas, S., Giabouranis, P., Yannopoulos, S. N., & Dracopoulos, V. (2007). Preparation of ZnO nanoparticles by thermal decomposition of zinc alginate. *Thin Solid Films*, *515*, 8461–8464.

Bobowska, I., Wojciechowski, P., & Halamus, T. (2008). Organic–inorganic nanocomposites of (2 hydroxypropyl) cellulose as a precursor of nanocrystalline zinc oxide layers. *Polymers for Advanced Technology*, *19*, 1860–2186.

Cao, B. Q., Cai, W. P., Li, Y., Sun, F. Q., & Zhang, L. D. (2005). Ultraviolet-light-emitting ZnO nanosheets prepared by a chemical bath deposition method. *Nanotechnology*, *16*, 1734–1738.

Chairam, S., Poolperm, C., & Somsook, E. (2009). Starch vermicelli template-assisted synthesis of size/shape-controlled nanoparticles. *Carbohydrate Polymers*, *75*, 694–704.

Carp, O., Huismann, C. L., & Reller, A. (2004). Photoinduced reactivity of titanium dioxide. *Progress in Solid State*, *32*, 33–177.

Chang, P. R., Yu, J., Ma, X., & Anderson, D. P. (2011). Polysaccharides as stabilizers for the synthesis of magnetic nanoparticles. *Carbohydrate Polymers*, *83*, 640–644.

Chen, M., Wang, X., Yu, Y. H., Pei, Z. L., Bai, X. D., Sun, C., et al. (2000). X-ray photoelectron spectroscopy and Auger electron spectroscopy studies of Al doped ZnO films. *Applied Surface Science*, *158*, 134–140.

Coperland, L., Blazek, J., Salam, H., & Chiming, T. M. (2009). Form and functionality of starch. *Food Hydrocolloid*, *23*, 1527–1534.

Decremps, F., Pellicer-Porres, J., Saitta, A. M., Chervin, J. C., & Polian, A. (2002). High-pressure Raman spectroscopy study of wurtzite ZnO. *Physical Review B*, *65*, 092101–092105.

Dijken, V. A., Meulenkamp, E., Vanmaekelbergh, D., & Meijerink, A. (2000). The kinetics of the radiative and nonradiative processes in nanocrystalline ZnO particles upon photoexcitation. *The Journal of Physical Chemistry B*, *104*, 1715–1723.

Djurišić, A. B., & Leung, Y. H. (2006). Optical properties of ZnO nanostructures. *Small*, *2*, 944–961.

Djurišić, A. B., Leung, Y. H., Tam, K. H., Ding, L., Ge, W. K., Chen, H. Y., et al. (2006). Green, yellow, and orange defect emission from ZnO nanostructures: Influence of excitation wavelength. *Applied Physics Letters*, *88*, 103107.

Gao, S., Zhang, H., Wang, X., Deng, R., Sun, D., & Zheng, G. (2006). ZnO-based hollow microspheres: Biopolymer-assisted assemblies from ZnO nanorods. *The Journal of Physical Chemistry B*, *110*, 15847–15852.

Ghoshal, T., Kar, S., & Chaudhuri, S. J. (2006). Synthesis and optical properties of nanometer to micrometer wide hexagonal cones and columns of ZnO. *Journal of Crystal Growth*, *293*, 438–446.

Greene, L. E., Law, M., Goldberger, J., Kim, F., Johnson, J. C., Zhang, Y., et al. (2003). Low-temperature wafer-scale production of ZnO nanowire arrays. *Angewewandte Chemie International Edition*, *42*, 3031–3034.

Imberty, A., Chanzy, H., Perez, S., Buleon, A., & Tran, V. (1988). The double-helical nature of the crystalline part of A-starch. *Journal of Molecular Biology*, *201*, 365–378.

Jiang, B., Tian, C., Zhou, W., Wang, J., Xie, Y., Pan, Q., et al. (2011). In situ growth of TiO_2 in interlayers of expanded graphite for the fabrication of TiO_2–graphene with enhanced photocatalytic activity. *Chemistry—A European Journal*, *17*, 8379–8387.

Hayat, K., Gondal, M. A., Khaled, M. M., Ahmed, S., & Shemsi, A. M. (2011). Nano ZnO synthesis by modified sol gel method and its application in heterogeneous photocatalytic removal of phenol from water. *Applied Catalysis A: General*, *393*, 122–129.

Jiang, P., Zhou, J. J., Fang, H. F., Wang, C. Y., Wang, Z. L., & Xie, S. S. (2007). Hierarchical shelled ZnO structures made of bunched nanowire arrays. *Advanced Functional Materials*, *17*, 1303–1310.

Jurca, B., Tirsoaga, A., Ianculescu, A., & Carp, O. (2014). Influence of the synthesis parameters on the thermal behaviour of some ZnO–starch composites. *Journal of Thermal Analysis and Calorimetry*, *115*, 495–501.

Kamalasanan, M. N., & Chandra, S. (1996). Sol–gel synthesis of ZnO thin films. *Thin Solid Films*, *288*, 112–115.

Kaukpetoom, D., & Wang, Y. J. (2001). Characterization of different starches oxidized by hypoclorite. *Starch Starke*, *53*, 211–218.

Kimball, J. W. (1994). *Biology* (6th ed.). Dubuque, Iowa: Addison-Wesley Pub. Co.

Lepot, N., Van Bael, M. K., Van den Rul, H., D'Haen, J., Peeters, R., Franco, D., et al. (2007). Synthesis of ZnO nanorods from aqueous solution. *Materials Letters*, *61*, 2624–2627.

Li, Z., Xiong, Y., & Xie, Y. (2005). Selective growth of ZnO nanostructures with coordination polymers. *Nanotechnology*, *16*, 2303–2308.

Liao, D. L., Badour, C. A., & Liao, B. Q. (2008). Preparation of nanosized TiO_2/ZnO composite catalyst and its photocatalytic activity for degradation of methyl orange. *Journal of Photochemistry and Photobiology A*, *194*, 11–19.

Li, Y., Wu, K., & Zhitomirsky, I. (2010). Electrodeposition of composite zinc oxide–chitosan films. *Colloids and Surfaces A: Physicochemical and Engineering Aspects*, *356*, 63–70.

Li, D., Lueng, I. H., Djurišić, B. A., Liu, Z. T., Xie, M. H., Shi, S. L., et al. (2004). Different origins of visible luminescence in ZnO nanostructures fabricated by the chemical and evaporation methods. *Applied Physics Letters*, *85*, 1601–1603.

Liu, J., Huang, X., Sulieman, K. M., Sun, F., & He, X. (2006). Solution-based growth and optical properties of self-assembled monocrystalline ZnO ellipsoids. *The Journal of Physical Chemistry B*, *110*, 10612–10618.

Łabanowska, M., Wesełucha-Birczyńska, A., Kurdziel, M., & Puch, P. (2013). Thermal effects on the structure of cereal starches. EPR and Raman spectroscopy studies. *Carbohydrate Polymers*, *92*, 842–848.

Lu, Q., Gao, F., & Komarneni, S. (2005). A green chemical approach to the synthesis of tellurium nanowires. *Langmuir*, *21*, 6002–6005.

Marinkivic, Z. V., Mancic, L., & Milosevic, O. (2004). The nature of structural changes in nanocrystalline ZnO powders under linear heating conditions. *Journal of the European Ceramic Society*, *24*, 1929–1933.

McKenzie, L., & Hutchison, J. (2004). Green nanoscience: An integrated approach to greener products, processes, and applications. *Chemistry Today*, *22*, 25–28.

Mo, M., Yu, J. C., Zhang, L., & Li, S. K. A. (2005). Self-assembly of ZnO nanorods and nanosheets into hollow microhemispheres and microspheres. *Advanced Materials*, *17*, 756–760.

Monticone, S., Tufeu, R., & Kanaev, A. V. (1998). Complex nature of the UV and visible fluorescence of ZnO nanoparticles. *The Journal of Physical Chemisty B*, *102*, 2854–2862.

Mumalo-Djokic, D., Stern, W. B., & Taubert, A. (2008). Zinc oxide/carbohydrate hybrid materials via mineralization of starch and cellulose in the strongly hydrated ionic liquid tetrabutylammonium hydroxide. *Crystal Growth & Design*, *8*, 330–335.

Nakamoto, K. (1986). *Infrared and Raman spectra of inorganic and coordination compounds*. New York: Wiley.

Pardeshi, S. K., & Patil, A. B. (2008). A simple route for photocatalytic degradation of phenol in aqueous zinc oxide suspension using solar energy. *Solar Energy*, *82*, 700–705.

Patrinoiu, G., Tudose, M., Calderón-Moreno, J. M., Birjega, R., Budrugeac, P., Ene, R., et al. (2012). A green chemical approach to the synthesis of photoluminescent ZnO hollow spheres with enhanced photocatalytic properties. *Journal of Solid State Chemistry*, *186*, 17–22.

Raveendran, P., Fu, J., & Wallen, S. L. (2003). Completely green synthesis and stabilization of metal nanoparticles. *Journal of the American Chemical Society*, *125*, 13940–13941.

Rodriguez-Gattorno, G., Santiago-Jacinto, P., Rendon-Vazquez, L., Nemeth, J., Dekany, I., & Diaz, D. (2003). Novel synthesis pathway of ZnO nanoparticles from the spontaneous hydrolysis of zinc carboxylate salts. *The Journal of Physical Chemistry B*, *107*, 12597–12604.

Somsook, E., Hinsin, D., Buakhrong, P., Teanchai, R., Mophan, N., Pohmakotr, M., et al. (2005). Interactions between iron(III) and sucrose, dextran, or starch in complexes. *Carbohydrate Polymers*, *61*, 281–287.

Sounart, T. L., Liu, J., Voigt, J. A., Hsu, J. W. P., Spoerke, E. D., Tian, Z. R., et al. (2006). Sequential nucleation and growth of complex nanostructured films. *Advanced Functional Materials*, *16*, 335–344.

Staroszczyk, H., & Janas, P. (2010). Microwave-assisted synthesis of zinc derivatives of potato starch. *Carbohydrate Polymers*, *80*, 962–979.

Sun, H. K., Luo, M., Weng, W. J., Cheng, K., Du, P. Y., Shen, G., et al. (2008). Room-temperature preparation of ZnO nanosheets grown on Si substrates by a seed-layer assisted solution route. *Nanotechnology*, *19*, 125603.

Thirumavalavan, M., Huang, K. L., & Lee, J. F. (2013). Synthesis and properties of nano ZnO using polysaccharides as chelating agents: Effects of various parameters on surface modification of polysaccharides. *Colloid Surface A*, *417*, 154–160.

Thoen, J., & Busch, R. (2006). Industrial chemicals from biomass—Industrial concepts. In B. Kamm, P. R. Gruber, & M. Kamm (Eds.), *Biorefineries—Industrial processes and products. Status quo and future directions. 2 Volumes. Practical approach book* (pp. 347–356). Weinheim: Wiley.

Trandafilović, L. V., Božanić, D. K., Dimitrijević-Branković, S., Luyt, A. S., & Djoković, V. (2012). Fabrication and antibacterial properties of ZnO–alginate nanocomposites. *Carbohydrate Polymers*, *88*, 263–269.

Vigneshwaran, N., Kumar, S., Kathe, A. A., Varadarajan, P. V., & Prasad, V. (2006). Functional finishing of cotton fabrics using zinc oxide–soluble starch nanocomposites. *Nanotechnology*, *17*, 5087–5095.

Vigneshwaran, N., Nachane, R. P., Balasubramanya, R. H., & Varadarajan, P. V. (2006). A novel one-pot 'green' synthesis of stable silver nanoparticles using soluble starch. *Carbohydrate Research*, *341*, 2012–2018.

Visinescu, D., Patrinoiu, G., Tirsoaga, A., & Carp, O. (2013). Polysaccharides routes: A new green strategy for metal oxides synthesis. In E. Lichtfouse, J. Schwarbauer, & D. Roberts (Eds.), *Environmental chemistry for a sustainable world* (pp. 119–172). Dordrecht Heidelbrg London New York: Springer.

Wang, Z., Cai, W., Hong, X., Zhao, X., Xu, F., & Cai, C. (2005). Photocatalytic degradation of phenol in aqueous nitrogen-doped TiO_2 suspensions with various light sources. *Applied Catalysis B: Environmental*, *57*, 223–231.

Wei, A., Sun, X. W., Xu, C. X., Dong, Z. L., Yang, Y., Tan, S. T., et al. (2006). Growth mechanism of tubular ZnO formed in aqueous solution. *Nanotechnology*, *17*, 1740–1744.

Xu, L. P., Hu, Y. L., Pelligra, C., Chen, C. H., Jin, L., Huang, H., et al. (2009). ZnO with different morphologies synthetized by solvothermal methods for enhaced photocatalytic activity. *Chemistry of Materials*, *21*, 2875–2885.

Yin, J., Lu, Q., Yu, Z., Wang, J., Pang, H., & Gao, F. (2010). Hierarchical ZnO nanorodassembled hollow superstructures for catalytic and photoluminescence applications. *Crystal Growth & Design*, *10*, 40–43.

Yu, J., Li, C., & Liu, S. (2008). Effect of PSS on morphology and optical properties of ZnO. *Journal of Colloid and Interface Science*, *326*, 433–438.

Zhang, Z., & Mu, J. (2007). Hydrothermal synthesis of ZnO nanobundles controlled by PEO-PPO-PEO block copolymers. *J. Colloid Interface Sci.*, *307*, 79–82.

Zheng, H., Duan, G., Li, Y., Yang, S., Xu, X., & Cai, W. (2010). Blue luminescence of ZnO nanoparticles based on non-equilibrium processes: Defect origins and emission controls. *Advanced Functional Materials*, *20*, 561–572.

Zheng, Y., Chen, C., Zhan, Y., Lin, X., Zheng, Q., Wei, K., et al. (2007). Luminescence and photocatalytic activity of ZnO nanocrystals: Correlation between structure and property. *Inorganic Chemistry*, *46*, 6675–6682.